Journal of Thermal Analysis and Calorimetry
https://doi.org/10.1007/s10973-025-14596-9

Thermal analysis of the components used in the fabrication of Al_2O_3–Ni and Al_2O_3–Mo composites via vat photopolymerization followed by spark plasma sintering

Joanna Tanska[1,2] · Mihai Alexandru Grigoroscuta[3] · Piotr Wiecinski[1] · Andrzej Ostrowski[1] · Oleg Vasylkiv[2] · Tohru S. Suzuki[2] · Paulina Wiecinska[1]

Received: 5 September 2024 / Accepted: 19 July 2025

Abstract

In this study, thermal analysis (including differential thermal analysis and thermogravimetric analysis coupled with mass spectrometry) was used to design the sintering process of alumina as well as Al_2O_3–Mo and Al_2O_3–Ni green bodies obtained by digital light processing (DLP) 3D printing. The measurements were performed for selected organic additives, which are commonly used in the DLP technique, such as photoinitiators, dispersing agents, and organic monomers. Additionally, metallic powders (Ni, Mo), as well as ceramic and composite green bodies, have been subjected to thermal analysis. The obtained results allowed us to determine proper sintering conditions for a two-step sintering program. Firstly, the organic phase was burnt out at 400 °C in the air. At this temperature, metallic powders have not yet started to oxidize, and most of the organic additives have already been eliminated from the sample. The second step was performed using spark plasma sintering at 1150 °C with a pressure equaling 60 MPa in an argon atmosphere to prevent the oxidation of metals. The samples were gradually cooled down to 800 °C at a cooling rate of 35 °C min^{-1} and then furnace-cooled to room temperature, preventing the formation of intrinsic defects (microcracks) in a multicomponent ceramic–metal composite. The XRD and SEM–EDS analysis allowed us to conclude that the obtained composites are well densified, no other phases apart from alumina and metals are present in the samples, and that the alumina grain growth is smaller than for conventional sintering. An increase in fracture toughness for the composite samples was observed compared to pure alumina.

✉ Paulina Wiecinska
paulina.wiecinska@pw.edu.pl

[1] Faculty of Chemistry, Warsaw University of Technology, 3 Noakowskiego St., 00-664 Warsaw, Poland

[2] National Institute for Materials Science (NIMS), 1-2-1 Sengen, Tsukuba, Ibaraki 305-0047, Japan

[3] National Institute of Materials Physics, Atomistilor Str. 405A, 077125 Bucharest, Magurele, Romania

Published online: 24 August 2025

Graphical abstract

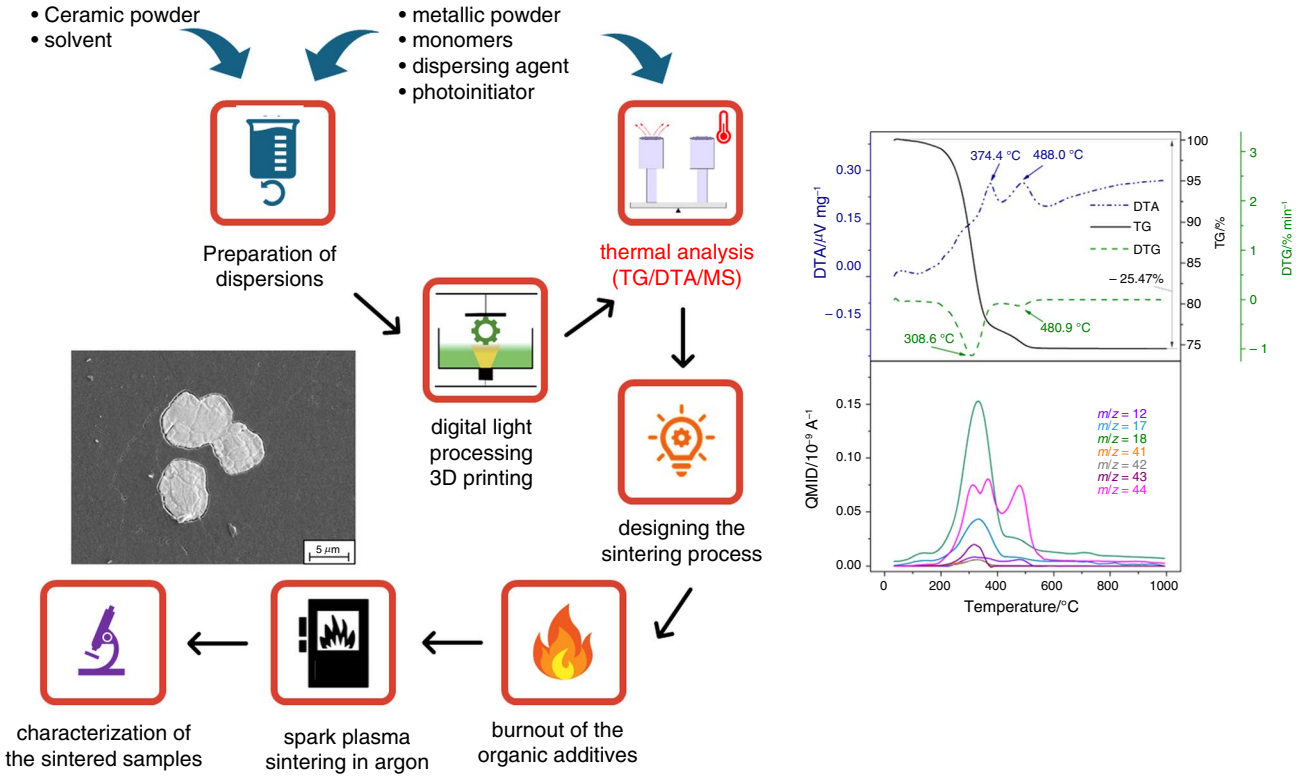

Keywords Thermal decomposition · Mass spectrometry · Vat photopolymerization · Spark plasma sintering · Ceramic–metal composites

Introduction

Among the methods of shaping ceramic matrix composites, additive manufacturing techniques are becoming more and more popular, as they allow to obtain precise and complex elements without the use of casting molds [1–4]. Digital light processing (DLP) 3D printing is a method belonging to the Vat Photopolymerization group, in which a photocurable dispersion of ceramic powder in liquid resin needs to be prepared [5]. The photosensitive suspension is then cured under a digital light projector screen during printing. In comparison with other 3D printing methods, Vat Photopolymerization offers many advantages, such as precise formation, smooth surface finish for printed samples, and simplified post-processing. Additionally, it allows the production of dense ceramics and is an excellent tool in manufacturing micro-sized elements. These qualities make DLP 3D printing appealing for the fabrication of ceramic and composite materials with complex geometries.

In the case of Vat Photopolymerization, the proper selection of organic additives plays a key role in the preparation of photocurable dispersions. Components, such as photoinitiators, organic monomers, dispersing agents, and solvents, are necessary to obtain the suspension with appropriate properties for DLP 3D printing, but the organic phase has to be eliminated during sintering in order to obtain well-densified pure ceramic or composite materials as a final product [6–8]. Because a lot of organic additives are used in the preparation of the dispersions, their content in the photocurable resin is usually about 45–60 vol%; thus, the debinding and sintering processes are a big challenge [9]. For example, a heating rate that is too high can result in delamination, deformation, and cracking of the material [10, 11]. Furthermore, in the case of the fabrication of ceramic–metal composites, it is important to select the sintering conditions in such a way to avoid the oxidation of metals [12].

Therefore, the sintering process needs to be adjusted to a specific material individually [13–15]. Thermogravimetric analysis allows to determine the temperature range at which the decomposition of selected additives separately, as well as in the ceramic and composite green bodies, occurs [16–19]. At DTA/TG measurements, the oxidation temperature of metallic powders can also be observed [20]. Additionally, with the use of mass

spectrometry, it is possible to indicate gases released during the decomposition of the organic compounds [21]. This information is very useful in determining the proper sintering conditions, such as heating rate, temperature, and atmosphere [15, 22–24]. Based on the literature data, spark plasma sintering (SPS) is a very effective technique for sintering of ceramic matrix composites, which allows to obtain well-densified materials at lower temperatures and shorter time of the sintering process [25–32].

According to the literature, in the ceramic–metal composites, an increase in fracture toughness is observed comparing to the monolithic ceramic materials [33]. This effect is caused by the fact that the cracks propagating in the ceramic matrix are blocked on the metallic particles. Exemplary mechanisms are crack deflection and crack blocking by plastic deformation. Ceramic–metal composites can find applications in cutting tools with increased durability, anti-corrosion covers, and construction material in nuclear power plants [34–36].

The aim of the research was to perform DTA/TG/DTG/MS analysis for the organic additives that are commonly used in Vat Photopolymerization, and for green bodies fabricated with their use, to establish proper sintering conditions for 3D-printed samples. In this study, pure alumina, Al_2O_3–Mo, and Al_2O_3–Ni composite samples were prepared using DLP 3D printing, followed by pressureless organic-phase decomposition in air and SPS in argon.

Materials and methods

Materials

Components commonly used in the Vat Photopolymerization process were selected for the analysis [37–42]. Four photoinitiators have been chosen: Omnirad 819 (IGM Resins), Omnirad 2100 (IGM Resins), Omnirad 2959 (BASF), and TPO (BASF). The thermal decomposition of two diacrylic monomers has been analyzed: triethylene glycol dimethacrylate—TEGDMA, and poly(propylene glycol) dimethacrylate—PPGDMA (both from Sigma-Aldrich). Chemical formulas of photoinitiators and monomers used in the research are presented in Fig. 1. Hypermer KD1 (Croda International Plc), which is a dispersing agent that uses the electrosteric mechanism to stabilize the ceramic suspensions, was examined. These components can be used to obtain ceramic and composite samples via Vat Photopolymerization techniques.

The ceramic powder used in this research was α-Al_2O_3 TM-DAR (Taimei Chemicals, Japan). Additionally, nickel and molybdenum micropowders (both from Createc, Poland, purity > 99%) were used to obtain Al_2O_3–Mo and Al_2O_3–Ni composite samples. The thermal characteristics of Ni and Mo powders were performed to determine the temperature at which the metals start to oxidize. The metallic particles can be classified as micropowders (with an average particle size by DLS of 9.3 µm for Ni and 13.4 µm for Mo). In comparison, alumina is a submicron-size powder (with an

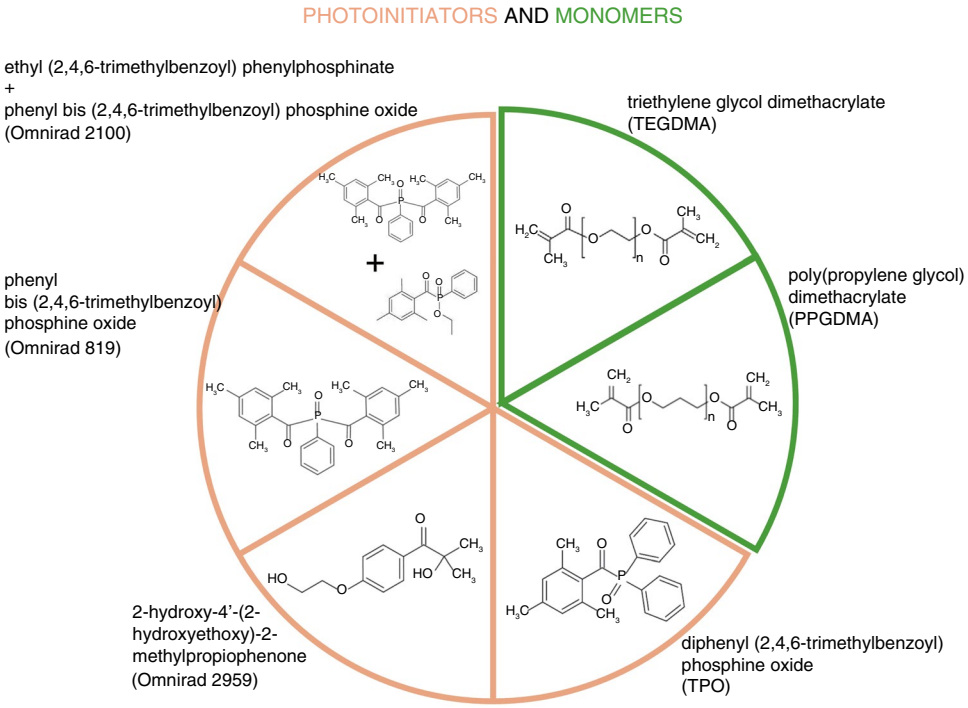

Fig. 1 Chemical formulas of monomers and photoinitiators used in the research

average particle size by DLS of 0.15 μm) that also influences the shaping process and the properties of the sintered bodies. All powders were of high purity, above 99%. The densities of the powders have been measured on a helium pycnometer AccuPyc II 1340 (Micromeritics), and they equal 3.9838 ± 0.035 g cm^{-3} for Al_2O_3, 8.7114 ± 0.0126 g cm^{-3} for Ni, and 9.8114 ± 0.0303 g cm^{-3} for Mo. The specific surface area S_{BET} was 11.5 m^2 g^{-1}, 0.31 m^2 g^{-1}, and 0.24 m^2 g^{-1} for alumina, nickel, and molybdenum, respectively.

Two different solvents were used to prepare ceramic suspensions: 2-ethylhexanol (Sigma-Aldrich) and an azeotropic mixture of trichloroethylene and ethanol (in a ratio 73:27).

Experimental

Two organic monomers (TEGDMA and PPGDMA) and the solvent (2-ethylhexanol) in a ratio 1:1:1 were mixed with the photoinitiator (Omnirad 2100) in a planetary ball mill Retsch PM200 for 15 min at 300 rpm. Meanwhile, the 50 mass% solution of KD1, in an azeotropic mixture of trichloroethylene and ethanol (in a ratio 73:27), was prepared by dissolving the dispersing agent in the solvent with the use of a magnetic stirrer for 15 min. Then, the solution of the deflocculant and the ceramic and metallic powders were added to the dispersion and were mixed for 30 min at 300 rpm, followed by 15 min of mixing at 350 rpm. The next step was carried out in order to remove air bubbles from the ceramic slurries. It included a two-step mixing and degassing process in a THINKY ARE-250 Mixing and Degassing Machine: mixing at a speed of 800 rpm for 2 min and degassing at 1800 rpm for 2 min. The program was repeated twice. Three series of suspensions have been prepared: Al_2O_3, Al_2O_3–Ni, and Al_2O_3–Mo. Table 1 shows the content of the components in the suspensions used in the DLP 3D printing process. All the slurries contained 45 vol% of alumina. The metallic content was 0.5 vol%.

The next step was obtaining cylindrical samples using a digital light processing FlashForge Hunter 3D printer equipped with a LED light projector that cures a slurry using a light beam with a wavelength of 405 nm. The light intensity equaled 4 mW cm^{-2} for ceramic suspensions and 5.2 mW cm^{-2} in the case of suspensions with the addition of nickel and molybdenum. The diameter of each sample was 10 mm, and their height was 5 mm. Samples were printed according to the previously prepared project in the Autodesk Fusion 360 program.

Simultaneous thermogravimetric analysis was carried out with the use of Netzsch Jupiter STA 449C coupled with the mass spectrometer Netzsch QMS 403C Aeolos. The measurements were performed for selected additives separately and for green bodies. The final temperature was 1000 °C, and the heating rate was 5 °C min^{-1}. All the samples were measured in the constant flow of two gases: argon—10 mL min^{-1} (protective gas), and synthetic air (75:25 N_2:O_2)—60 mL min^{-1}. Additionally, Al_2O_3–Mo and Al_2O_3–Ni samples were measured in argon only (in flow rate 50 mL min^{-1}). The samples in the quantities between 0.03 g and 0.21 g were placed in the crucibles together with c.a. 0.25 g of calcinated Al_2O_3 to prevent the overflowing of samples from the crucibles. TG/DTA/MS measurements helped to establish the sintering program.

To avoid the oxidation of metals in the composite samples during sintering, this process was divided into two steps. At first, the organic phase was burned out at 400 °C/2 h (heating rate 2 °C min^{-1}). This step was necessary because the printed green bodies contained a large amount of organic additives. The high heating rate in the SPS process (the initial stage of SPS is rapid temperature ramping from room temperature to over 700 °C) results in rapid decomposition of the organic phase that may cause an explosion of samples in the graphite matrix. The second step was spark plasma sintering of samples in argon at the temperature of 1150 °C/10 min (heating rate 50 °C min^{-1}) with the pressure equaling 60 MPa. The cooling process was performed without pressure. The samples were gradually cooled down to 800 °C at a cooling rate of 35 °C min^{-1} and then furnace-cooled to room temperature, which

Table 1 Composition of the dispersions used to obtain samples by DLP 3D printing

Component/ name of series	Al_2O_3	Al_2O_3–Ni	Al_2O_3–Mo
Al_2O_3 / vol%	45	45	45
2-ethylhexanol / vol% TEGDMA / vol% PPGDMA / vol%	55 (mol ratio 1:1:1)	55 (mol ratio 1:1:1)	55 (mol ratio 1:1:1)
KD1 / mass%*	1.5	1.5	1.5
Omnirad 2100 / mass%**	3	3	3
Ni / vol%	–	0.5	–
Mo / vol%	–	–	0.5

* With respect to the alumina content

** With respect to the monomers content

prevents the formation of intrinsic defects (microcracks) in a multicomponent ceramic–metal composite.

The densities of samples were measured using the Archimedes method in water. To check Vickers' hardness and fracture toughness, five indentations for each sample were made using Digital Vickers Hardness Tester HVS-30 T (Huatec Group Corporation) with a load of 29.4 N (3 kgf) applied for 10 s. Nikon Eclipse LV150N light microscope was used to measure the diagonals and cracks of each indentation. The fracture toughness has been calculated according to the Lankford equation [43]. The samples were thermally etched at 1200 °C for 15 min, and their microstructure was analyzed using a ThermoFisher Helios 5 PFIB scanning electron microscope. SEM observations allowed to determine the grain size of the ceramic matrix and the size of the metallic particles. Powder X-ray diffraction patterns were recorded at room temperature on a Bruker D8 Advance diffractometer equipped with a LYNXEYE position-sensitive detector, using Cu–Ka radiation (l = 0.15418 nm). The data were collected in the Bragg–Brentano (q/q) horizontal geometry (flat reflection mode) between 8 and 90° (2q) in a continuous scan, using 0.03° steps and 3 s/step (total time 576 s/step). The diffractometer incident beam path was equipped with a 2.5° Soller slit, and a 1.14° fixed divergence slit, while the diffracted beam path was equipped with a programmable antiscatter slit (fixed at 2.20°), a Ni β-filter, and a 2.5° Soller slit. Data were collected under standard laboratory conditions (temperature and relative humidity). The Diffrac.Eva program (Bruker AXS, Karlsruhe, Germany) and powder data of X-ray patterns from the PDF-2 database (by ICDD) were used to identify phases. Measurements were performed for sintered Al_2O_3–Ni and Al_2O_3–Mo samples. The samples were crushed before measurement, resulting in a powder with large grains.

Results and discussion

Thermal analysis has been performed for selected additives that are commonly used in the Vat Photopolymerization techniques: four photoinitiators (Omnirad 819, Omnirad 2100, Omnirad 2959, and TPO), two organic monomers (PPGDMA and TEGDMA), and a dispersing agent (KD1). The results of the measurements are presented in Figs. 2–4.

Figure 2a shows DTA/TG/DTG/MS curves of Omnirad 819 thermal degradation. According to the TG curve, the total mass loss was 82%, and the decomposition takes place in two main stages. It begins at ca. 145 °C and ends at ca. 695 °C. On the DTA curve, the exothermic peaks with the maxima at 193, 409, and 506 °C are visible. The first stage ends at 330 °C with 49% mass loss and is related to the release of CO_2, which indicates MS 44. In the second stage, the 33% mass loss is observed till 695 °C and is connected to the increase in all MS signals, which are 12, 17, 18, and 44. The mass loss can be the result of the overlap of two effects: decomposition of the hydrocarbon chain and oxidation reaction with the release of CO_2 (MS 12 and 44) and H_2O (MS 17 and 18).

Figure 2b presents the thermal decomposition of Omnirad 2100, which begins at 112 °C and ends at 712 °C with the total mass loss equaling 83%. Two main stages of Omnirad 2100 degradation are observed: the first stage till 331 °C connected with 47% mass loss and the second stage till 738 °C with 36% mass loss. At first, MS 17 and MS 18 signals are visible, which can be ascribed to OH^+ and H_2O^+ ions. Then, the increase in the values of m/z: 12, 44, and 51 begins. This effect is caused by benzene ring cleavage followed by the oxidation of its products to CO_2. The MS 51 signal indicates the presence of $C_4H_3^+$ [44, 45].

Figure 2c shows the DTA/TG/DTG/MS curves of Omnirad 2959. The total mass loss was 100%, what indicates that the whole photoinitiator has decomposed. The first stage of the process starts at 164 °C and ends at 327 °C with 69% mass loss. The second part of the decomposition is observed till 532 °C with 31% mass loss. The endothermic peak on the DTA curve with a minimum at 100 °C and the exothermic peak with a maximum at 498 °C are visible. According to the MS curves, the oxidation process, leading to the formation of H_2O, dominates at lower temperatures, which indicates MS 17 and 18. When the temperature exceeds 400 °C, the intensity of the peaks (MS 12 and 44) related to the decomposition of the compound and oxidation to CO_2 increases. Also, a small signal m/z = 43 corresponding to the release of light hydrocarbons is visible. Omnirad 2959 is the only photoinitiator among the ones selected for the research that decomposed in 100%. This is probably caused by the absence of phosphorus in its chemical structure.

DTA/TG/DTG/MS curves for TPO are presented in Fig. 2d. The decomposition of this compound goes in two stages: First, with a mass loss of 59%, starts at 239 °C, and second, with a mass loss of 26%, begins at 414 °C and ends at 769 °C. The total mass loss equaled 85%. One endothermic peak on the DTA curve with the minimum at 100 °C and two exothermic peaks with the maxima at 267 °C and 549 °C are visible. MS signals with the biggest intensity are related to the decomposition and oxidation processes toward H_2O and CO_2 (m/z values 17, 18, and 44). Several smaller peaks on the MS curve are also observed: MS 37, 38, 39, 51, 76, and 77. These signals correspond to the products of aromatic rings cleavage, such as C_3H^+, $C_3H_2^+$, $C_3H_3^+$, $C_4H_3^+$, $C_6H_4^+$, and $C_6H_5^+$.

Figure 3 shows the thermal decomposition of two organic monomers used in the research: poly(propylene glycol) dimethacrylate—PPGDMA, and triethylene glycol dimethacrylate—TEGDMA. The total mass loss for both tested compounds was 100%, indicating that the whole TEGDMA

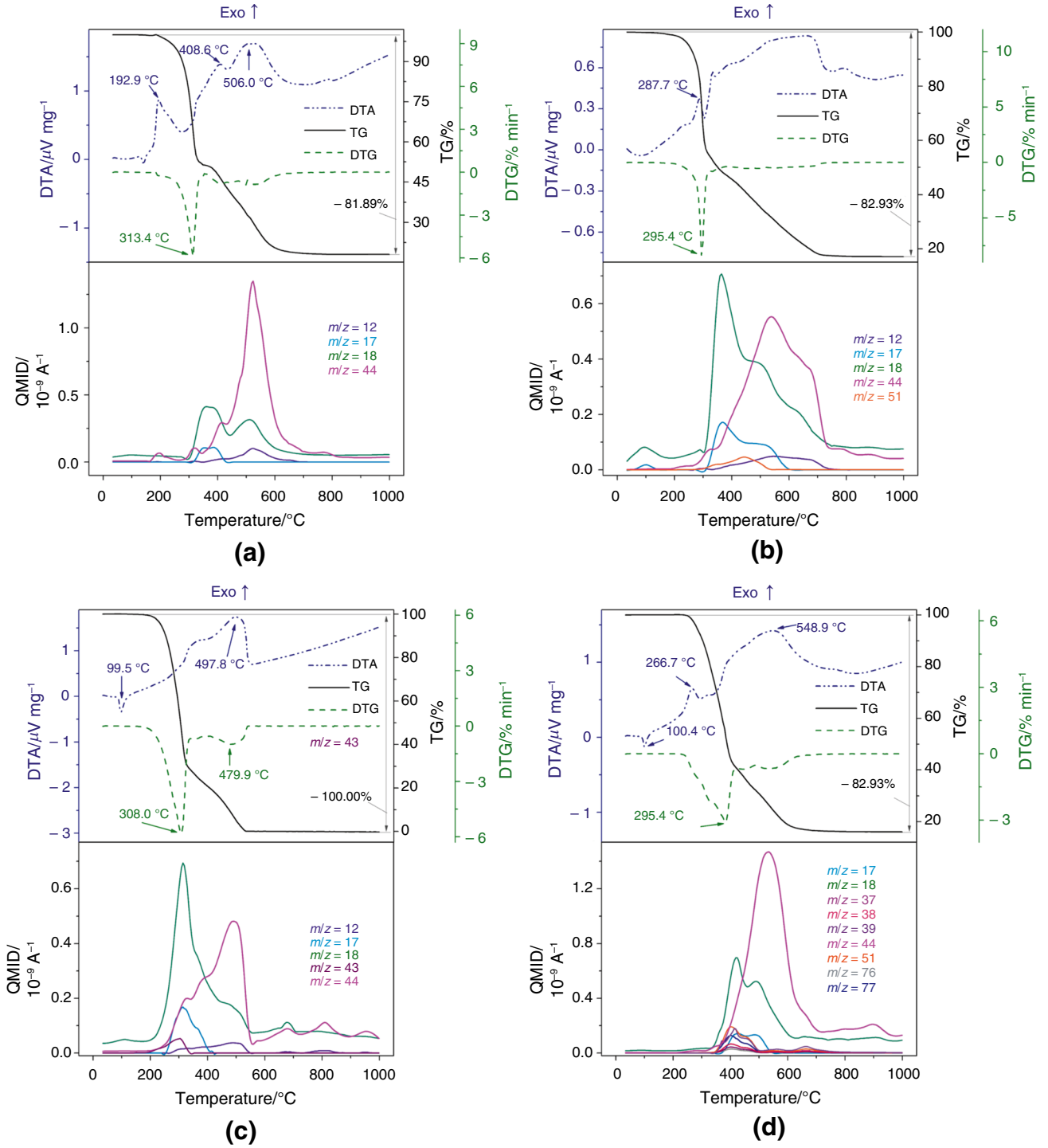

Fig. 2 DTA/TG/DTG curves and signals from mass spectrometer of 4 different photoinitiators in air: **a** Omnirad 819, **b** Omnirad 2100, **c** Omnirad 2959, **d** TPO

and PPGDMA have decomposed. For PPGDMA (Fig. 2a), two exothermic peaks with the maxima at 424 °C and 488 °C are visible, and the m/z values detected by mass spectrometer are as follows: 17, 18 (H_2O^+ and OH^+), 29 ($CH_3CH_2^+$), 41, 42, 43 (light hydrocarbons), 12 44 (CO_2). For all MS values, narrow peaks are observed at 361 °C, where the most significant mass loss is observed on the TG curve. For MS 44, there is also a small peak at ca. 485 °C, indicating that the compound's decomposition goes in two stages. The process is similar for TEGDMA (Fig. 2b) but takes place at

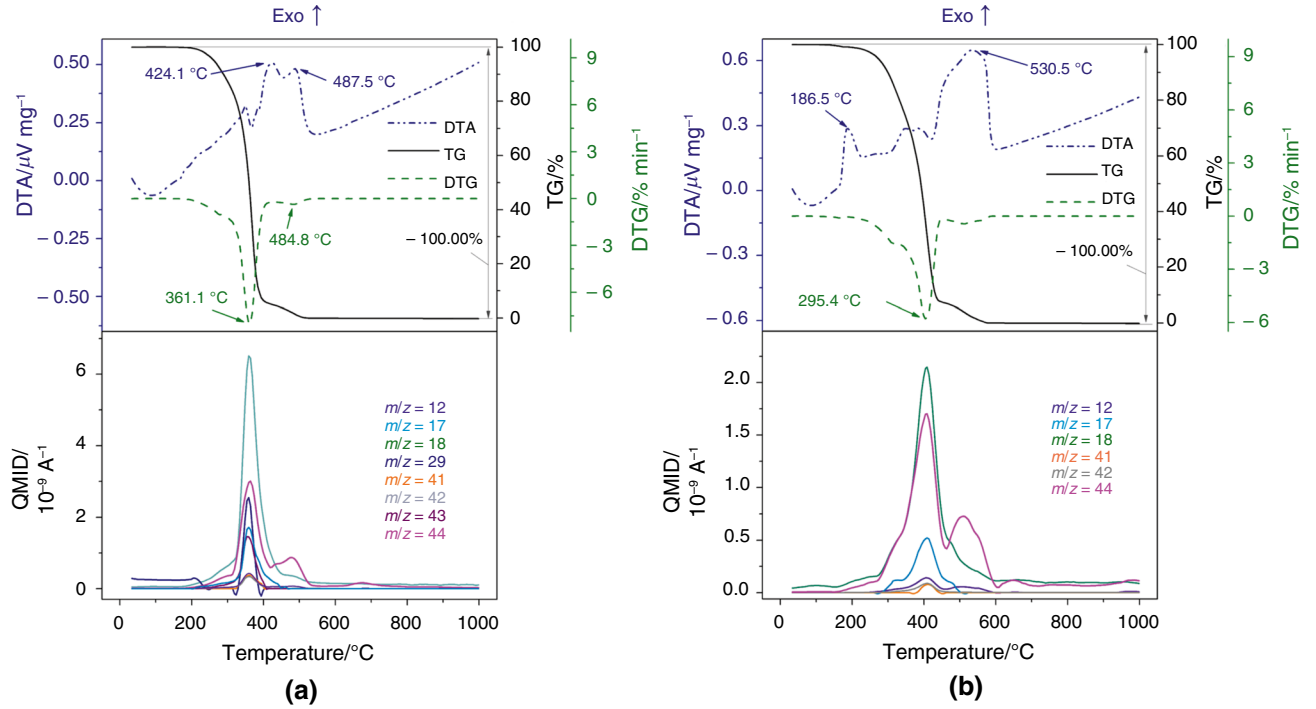

Fig. 3 DTA/TG/DTG curves and signals from mass spectrometer of **a** PPGDMA, **b** TEGDMA in air

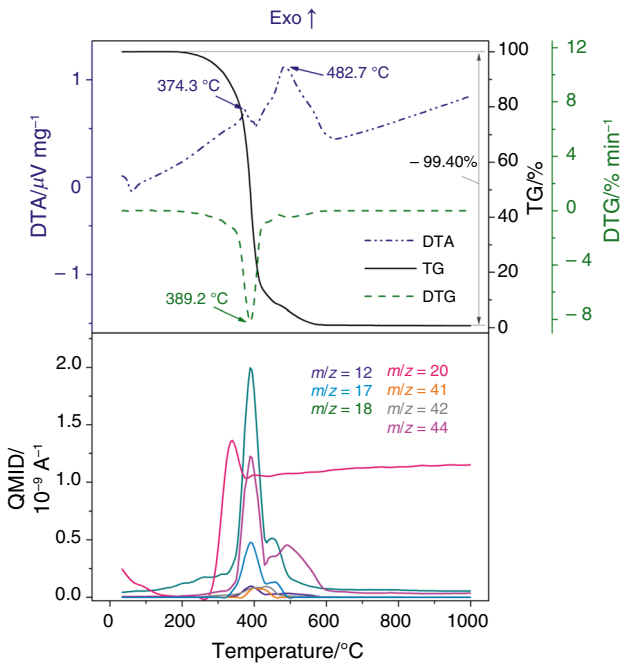

Fig. 4 DTA/TG/DTG curves and signals from mass spectrometer of KD1 in air

higher and wider temperature range with peaks at 405 °C and 530 °C and detected m/z values: 12, 44 (CO_2), 17, 18 (H_2O^+ and OH^+), and 41, 42 (light hydrocarbons).

Figure 4 presents the DTA/TG/DTG/MS curves of the KD1 dispersing agent. The total mass loss was 99%, what indicates that the whole KD1 has decomposed. On the DTA curve, two exothermic peaks with the maxima at 374 °C and 483 °C are visible. The first DTA peak corresponds to the DTG peak and MS peaks for m/z = 12, 44 (CO_2), 17, 18 (H_2O^+ and OH^+), 20, 41, 42 (light hydrocarbons) observed at ca. 390 °C. The second DTA peak corresponds to the wide peak observed at MS 44 at ca 480 °C, which indicates that the decomposition of KD1 is a two-stage process.

Figure 5 shows DTA/TG/DTG/MS curves of thermal degradation of alumina green sample obtained by DLP 3D printing with the use of the selected additives: Omnirad 2100, TEGDMA, PPGDMA, and KD1. The content of the components in the suspensions is presented in Table 1. The total mass loss was 25% which corresponds to the organic additives content in the analyzed sample. It means that all of the organic phases were burned out, as expected (leaving phosphorus from Omnirad 2100). The first stage of the process starts at 111 °C and ends at 387 °C with 22.8% mass loss. The second part of the decomposition is observed till 531 °C with 2.6% mass loss. The m/z values detected by the mass spectrometer are as follows: 17, 18 (H_2O^+ and OH^+), 12, 44 (CO_2), and 41, 42, 43 (light hydrocarbons). For all MS values, peaks are observed at ca. 310 °C, where the biggest mass loss is observed on the TG curve. For MS 12 and 44 (signals related to the release of CO_2), there is also a peak

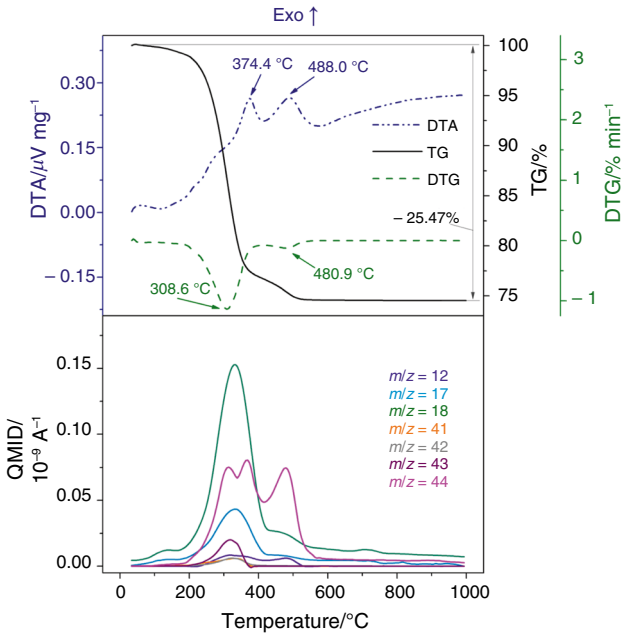

Fig. 5 DTA/TG/DTG curves and signals from mass spectrometer of Al_2O_3 green sample in air

at ca. 490 °C, which confirms that the sample's decomposition goes in two stages.

Figure 6 presents DTA/TG/DTG curves of molybdenum and nickel metallic powders conducted in air. These measurements allow to determine at what temperature the metal oxidation process occurs. For molybdenum powder (Fig. 6a), the process starts at 430 °C and ends at 660 °C with an increase in mass by 49%, what indicates the oxidation toward MoO_3. For nickel powder (Fig. 6b), the process starts at 400 °C and ends at 910 °C with an increase in mass by 26%, what indicates the oxidation toward NiO.

Figures 7 and 8 show DTA/TG/DTG/MS curves of thermal degradation of Al_2O_3–Mo and Al_2O_3–Ni green samples obtained by DLP 3D printing. The content of the components in the suspensions used to prepare the samples is presented in Table 1. The composite samples were measured separately in air and argon. For both samples measured in air (Figs. 7a and 8a), MS signals with the most considerable intensity are related to the decomposition and oxidation processes toward H_2O and CO_2 (m/z values 12, 17, 18, and 44); there is also a much smaller peak MS 29 ($CH_3CH_2^+$). A double, broad peak observed for m/z = 44 indicates that the decomposition of samples in air goes in two stages. The total mass loss was 23% for Al_2O_3–Mo and 21% for Al_2O_3–Ni. For both samples, on TG/DTG curves, a slight increase in mass can be observed (at 549 °C for Al_2O_3–Mo and at 509 °C for Al_2O_3–Ni), which is related to the oxidation of metallic particles in the air.

Sintering samples in argon (Figs. 7b and 8b) allows to avoid the oxidation of metallic particles but results in different products of the organic phase decomposition. For Al_2O_3–Mo sample, the m/z values detected by mass spectrometer are as follows: 17, 18 (H_2O^+ and OH^+), 15 (CH_3^+) 29 ($CH_3CH_2^+$), 43 (light hydrocarbons), 44 (CO_2). MS signals observed for Al_2O_3–Ni sample are 12, 44 (CO_2), 29 ($CH_3CH_2^+$), 26, 42 (light hydrocarbons). The total mass loss was 21% for Al_2O_3–Mo and 24% for Al_2O_3–Ni.

The obtained results show that the sintering of composite samples containing metallic particles should consist of two stages. Firstly, the decomposition of the organic phase should be performed in air to minimize the amount of toxic gases released during the process and to prevent the presence of residual carbon in the samples. The final temperature of the first step of the process cannot be higher than the temperature at which metals start to oxidize, what means that for molybdenum and nickel powders, it cannot be higher

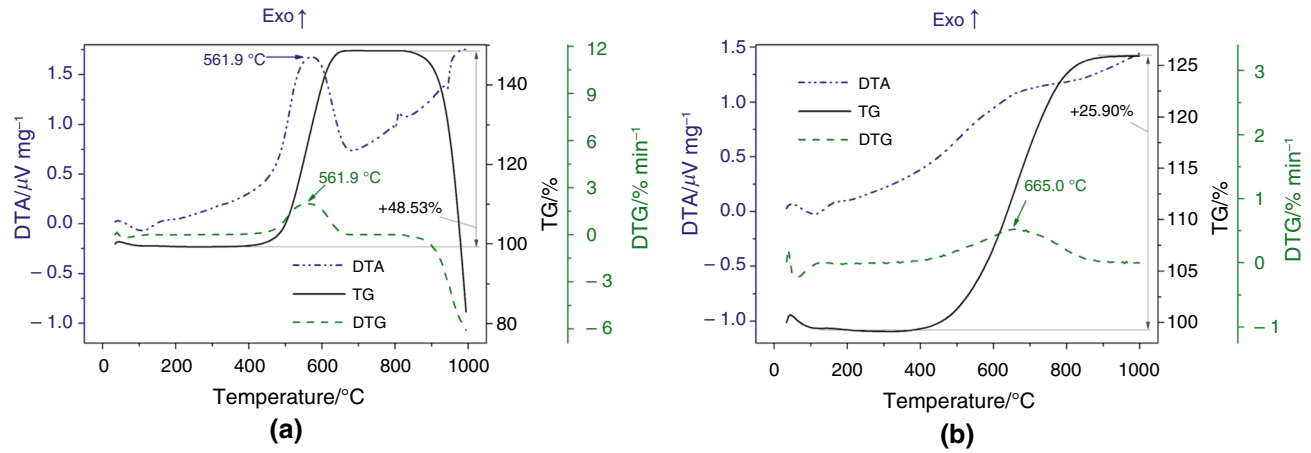

Fig. 6 DTA/TG/DTG curves of metallic powders in air **a** Mo, **b** Ni

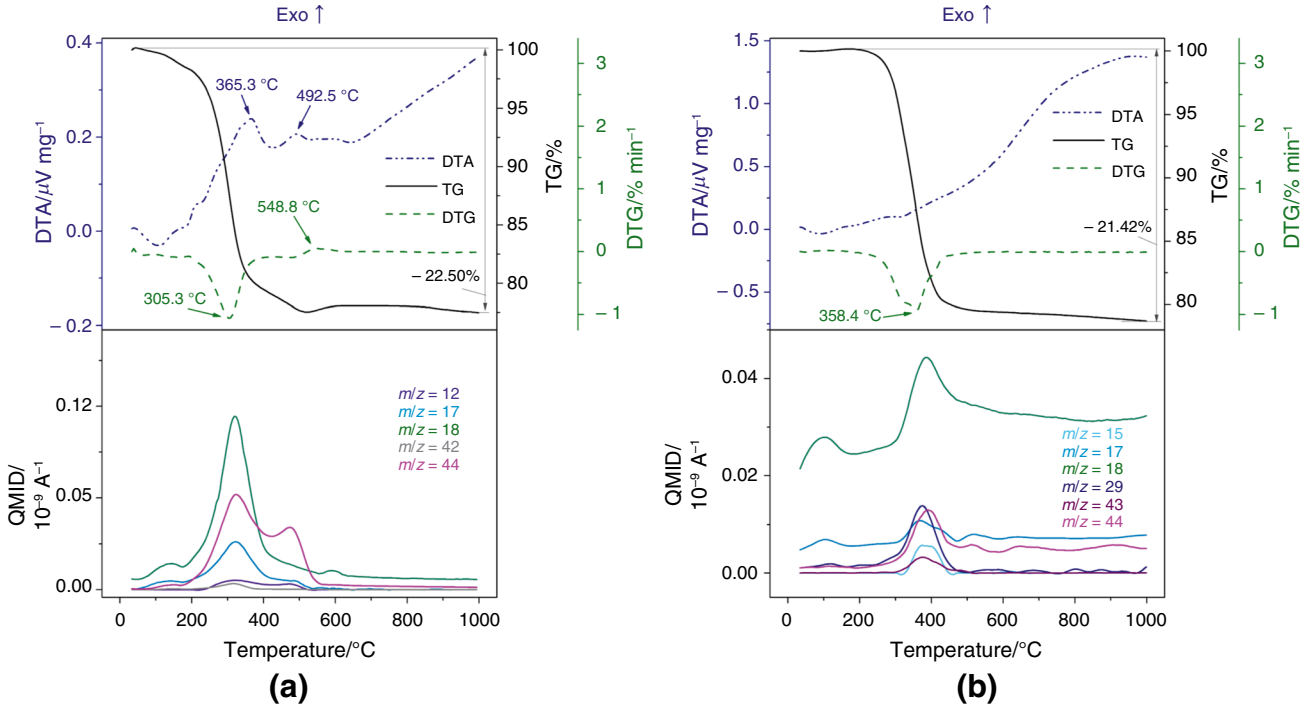

Fig. 7 DTA/TG/DTG curves and signals from mass spectrometer of Al_2O_3–Mo green sample **a** in air, **b** in argon

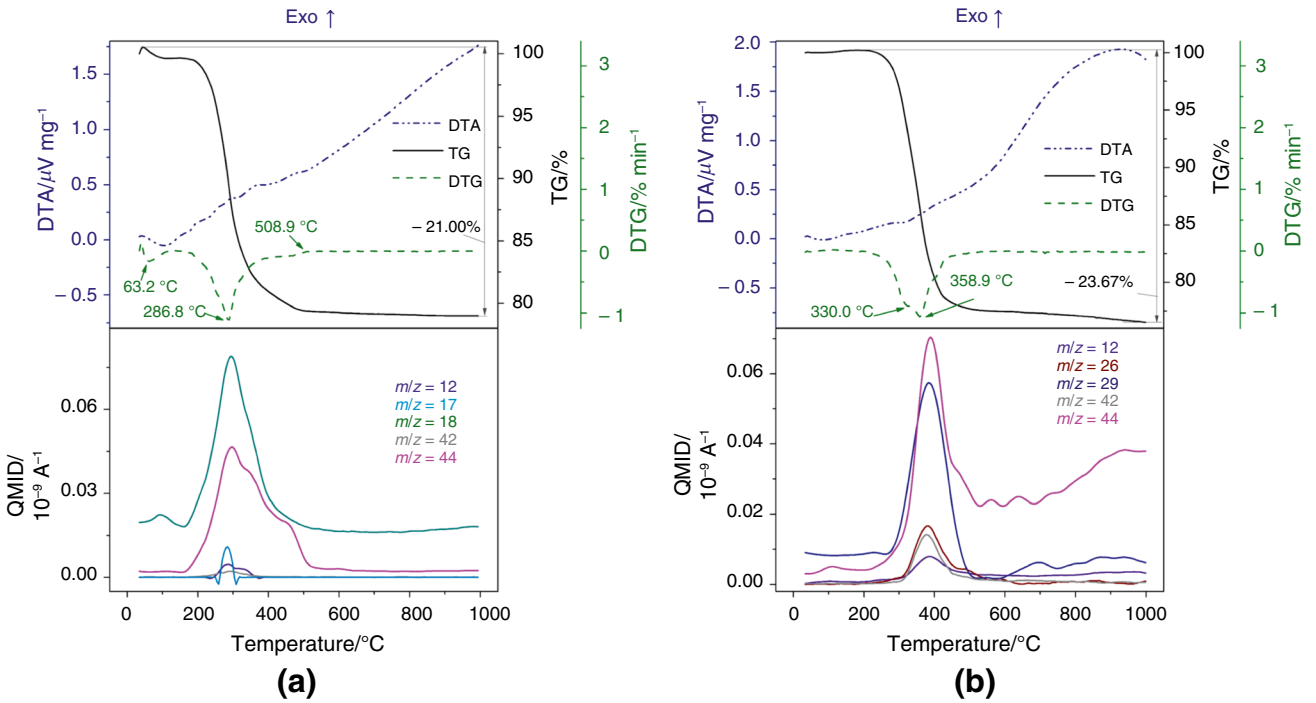

Fig. 8 DTA/TG/DTG curves and signals from mass spectrometer of Al_2O_3–Ni green sample **a** in air, **b** in argon

Table 2 Selected properties of green and sintered samples

Parameter	Al_2O_3	Al_2O_3–Ni	Al_2O_3–Mo
Relative density of green samples / % of theoretical density	61.74	61.35	61.54
Relative density of sintered samples / % of theoretical density	99.58	94.16	90.27
Volumetric shrinkage / %	67.90	54.88	56.65
Vickers hardness / GPa	21.36 ± 0.78	17.15 ± 1.32	17.24 ± 0.75
K_{IC} / MPa $m^{0.5}$	6.31 ± 0.16	6.58 ± 0.18	6.60 ± 0.37

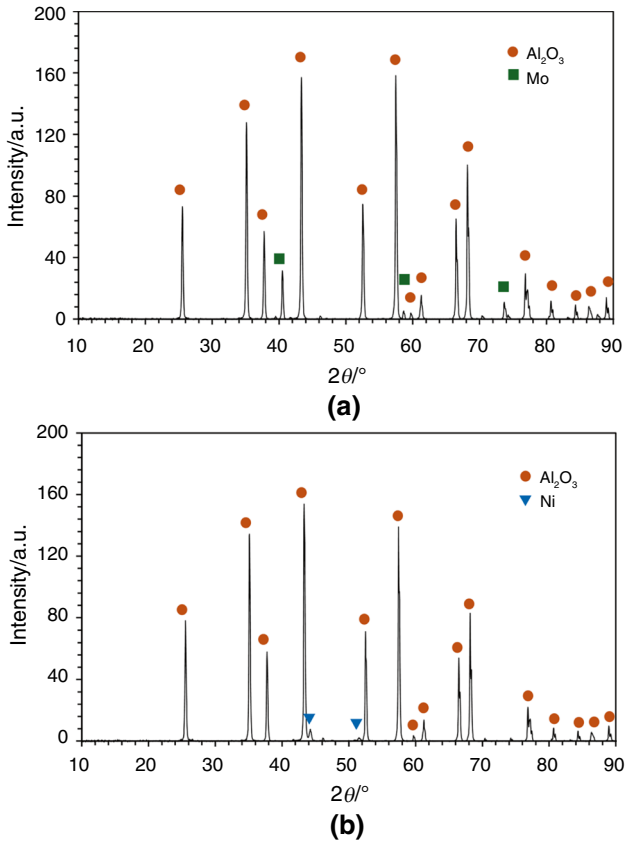

Fig. 9 XRD patterns for sintered samples: **A** Al_2O_3–Mo and **B** Al_2O_3–Ni

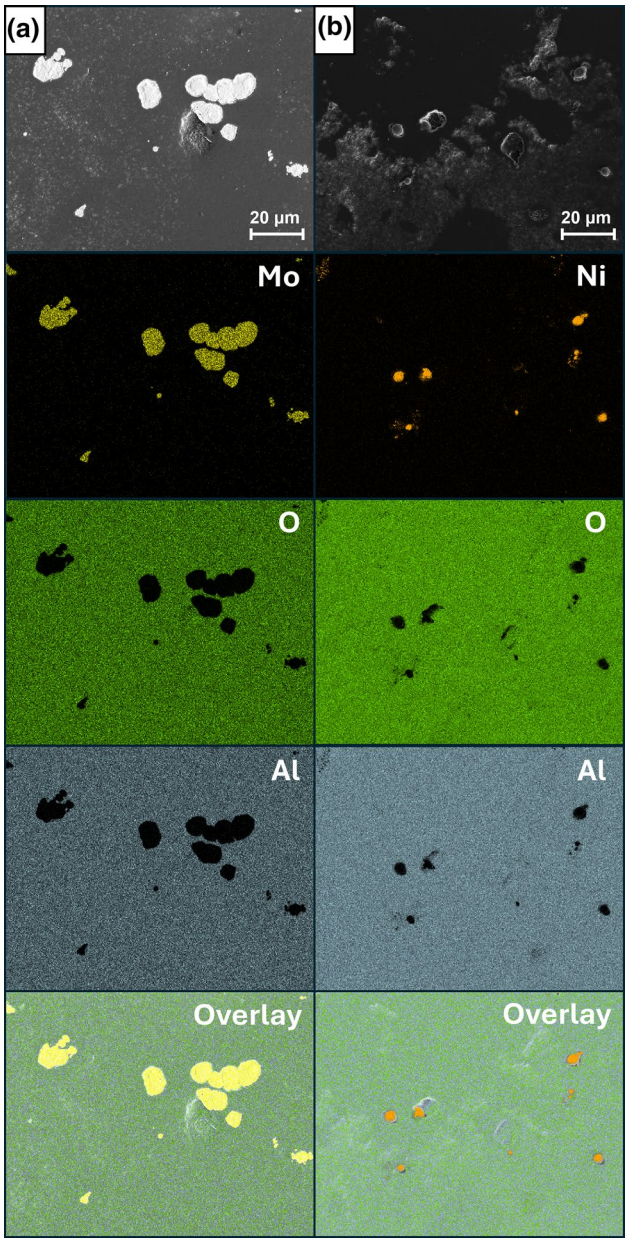

Fig. 10 SEM–EDS element mapping images of the obtained composite samples sintered in SPS

than 400 °C. Then, the samples should be sintered in argon to avoid the oxidation of metallic particles.

Samples obtained by DLP 3D printing have been characterized in terms of relative density, volumetric shrinkage, Vickers hardness, and fracture toughness K_{IC}. The results of the measurements of selected properties of green and sintered samples are presented in Table 2. The relative densities of the samples were then determined in both green and sintered states. The highest density was observed for the pure alumina sample. For sintered samples obtained with the addition of the metallic phase, a decrease in the relative density values was observed, and it equaled ca. 5% for the Al_2O_3–Ni sample and ca. 9% for Al_2O_3–Mo sample compared to the pure alumina sample. The volumetric shrinkage values were between 54.88% (Al_2O_3–Ni) and 67.90% (Al_2O_3). The samples with the addition of metallic phase were characterized by lower values of Vickers hardness than single–phase alumina samples (21.36 GPa, 17.15 GPa, and 17.24 GPa for Al_2O_3, Al_2O_3–Ni, and Al_2O_3–Mo samples, respectively). Metals are characterized by lower hardness than ceramics, so such an effect was expected [33, 46]. The

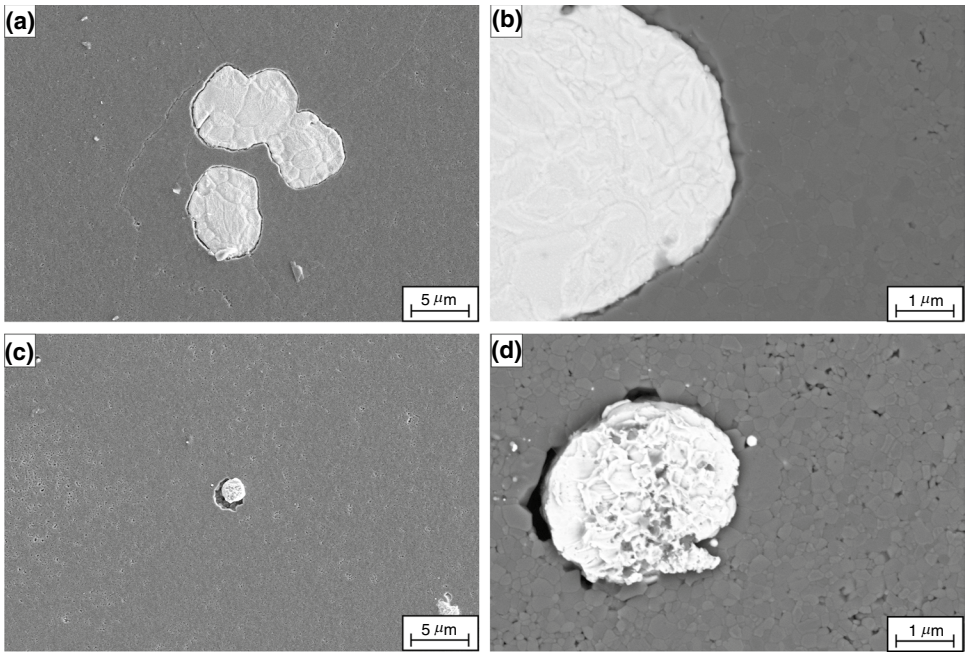

Fig. 11 SEM images of composites sintered in SPS: Al_2O_3–Mo (**A**, **B**) and Al_2O_3–Ni (**C**, **D**)

fracture toughness was calculated according to the Lankford equation. The composite samples' KIC increased by approximately 4 to 5% compared to single-phase alumina.

The results of the XRD analysis of Al_2O_3–Mo and Al_2O_3–Ni sintered samples showed that no other phases apart from alumina and metals are present in the printed composite objects (Fig. 9). It can be concluded that the two-step sintering program (burnout of the organic phase at 400 °C in air and sintering in argon at the temperature of 1150 °C) selected based on DTA/TG/DTG/MS analysis allows maintaining the composite's metallic phase without oxidation and spinel phase formation.

Figures 10 and 11 show SEM micrographs and EDS maps for Al_2O_3–Mo and Al_3O_3–Ni samples. The presence of the metallic particles in both samples indicates that the selection of temperatures and atmospheres of the organic phase decomposition and sintering processes, based on DTA/TG/MS measurements, allowed to avoid the oxidation of the metallic phase. The alumina grains in the ceramic matrix are in the range of 0.1–0.5 μm, so the grain growth is smaller than for conventional sintering. The metallic grains are bigger, what is an outcome of the starting powders used in the research, and their size is in the range of 2–5 μm for Mo and 1–2 μm for Ni grains.

Conclusions

Thermal decomposition of selected organic additives, which are commonly used in DLP 3D printing of ceramic materials and composites, has been performed. Four photoinitiators (Omnirad 819, Omnirad 2100, Omnirad 2959, and TPO), two organic monomers (PPGDMA and TEGDMA), and one dispersing agent (KD1) have been chosen for the analysis. Additionally, metallic powders (Ni, Mo) as well as ceramic (Al_2O_3) and composite (Al_2O_3–Mo, Al_2O_3–Ni) green bodies have been subjected to DTA/TG/MS measurements, which allowed us to characterize their decomposition process. Furthermore, the sintering process of the composite samples has been established on the basis of the obtained results. The first step, which consisted of burning out the organic phase in air, was performed at 400 °C. This is a temperature at which the majority of organic additives are removed, and the molybdenum and nickel powders do not yet start to oxidize. The second step of the sintering process was performed by SPS in an argon atmosphere, at 1150 °C with the pressure equaling 60 MPa, and it allowed to obtain Al_2O_3–Ni and Al_2O_3–Mo composites with improved K_{IC} in comparison to pure alumina. The XRD and SEM–EDS analysis allowed to conclude that the obtained composites are well densified, no other phases apart from alumina and metals are present in the samples and that the alumina grain growth is smaller than for conventional sintering.

Acknowledgements J. Tanska is grateful for the support from National Institute for Materials Science by the NIMS Internship Program. Research was partially funded by the Warsaw University of Technology within the Excellence Initiative: Research University (IDUB) program.

Author contributions Joanna Tanska was involved in investigation, writing—original draft, methodology, and data curation. Mihai Alexandru Grigoroscuta contributed to investigation and methodology. Piotr Wiecinski was involved in investigation (SEM observations) and validation. Andrzej Ostrowski contributed to investigation (XRD measurements). Oleg Vasylkiv was involved in conceptualization, writing—review and editing, and supervision. Tohru S. Suzuki

contributed to methodology and supervision. Paulina Wiecinska was involved in conceptualization, writing—review and editing, resources, and supervision.

References

1. Zhou S, Liu G, Wang C, Zhang Y, Yan C, Shi Y. Thermal debinding for stereolithography additive manufacturing of advanced ceramic parts: a comprehensive review. Mater Des. 2024;238:112632. https://doi.org/10.1016/j.matdes.2024.112632.
2. Fournier S, Chevalier J, Baeza GP, Chaput C, Louradour E, Sainsot P, et al. Ceria-stabilized zirconia-based composites printed by stereolithography: impact of the processing method on the ductile behaviour and its transformation features. J Eur Ceram Soc. 2023;43:2894–906. https://doi.org/10.1016/j.jeurceramsoc.2022.11.006.
3. Maillard M, Chevalier J, Gremillard L, Baeza GP, Courtial EJ, Marion S, et al. Optimization of mechanical properties of robocast alumina parts through control of the paste rheology. J Eur Ceram Soc. 2023;43:2805–17.
4. Bernard M, Pateloup V, Passerieux D, Cros D, Madrangeas V, Chartier T. Feasibility of manufacturing of Al2O3–Mo HTCC by hybrid additive process. Ceram Int. 2022;48:14993–5005.
5. Wang K, Qiu M, Jiao C, Gu J, Xie D, Wang C, et al. Study on defect-free debinding green body of ceramic formed by DLP technology. Ceram Int. 2020;46:2438–46.
6. Li Y, Sheng P, Lin L, Wang L, Lu D, Lin K, et al. Vat photopolymerization versus conventional colloidal processing methods in structural ceramics: progress, challenges, and future perspectives. Addit Manuf Front. 2024;3:200110. https://doi.org/10.1016/j.amf.2024.200110.
7. Stögerer J, Baumgartner S, Rath T, Stampfl J. Analysis of the mechanical anisotropy of stereolithographic 3D printed polymer composites. Eur J Mater. 2022;2:12–32. https://doi.org/10.1080/26889277.2022.2035196.
8. Falkowski P, Żurowski R. Shaping of alumina microbeads by drop-casting of the photopolymerizable suspension into silicone oil and UV curing. J Eur Ceram Soc. 2022;42:3957–67.
9. Zeng Y, Chen X, Sun L, Yao H, Chen J. Effect of different sintering additives type on vat photopolymerization 3D printing of Al2O3 ceramics. J Manuf Process. 2022;83:414–26.
10. Li H, Liu YS, Liu YS, Zeng QF, Hu KH, Liang JJ, et al. Microstructure and properties of 3D-printed alumina ceramics with different heating rates in vacuum debinding. Rare Met. 2020;39:577–88.
11. Trunec M, Cihlar J. Thermal removal of multicomponent binder from ceramic injection mouldings. J Eur Ceram Soc. 2002;22(13):2231–41.
12. Zygmuntowicz J, Wiecinska P, Miazga A, Konopka K, Szafran M, Kaszuwara W. Thermoanalytical studies of the ceramic-metal composites obtained by gel-centrifugal casting. J Therm Anal Calorim. 2018;133:303–12.
13. Li H, Liu Y, Liu Y, Zeng Q, Hu K, Lu Z, et al. Effect of sintering temperature in argon atmosphere on microstructure and properties of 3D printed alumina ceramic cores. J Adv Ceram. 2020;9:220–31.
14. Valdes-Tabernero MA, Monclus MA, Sabirov I, Molina-Aldareguia JM, Petrov RH, Wang J, et al. The effect of ultrafast heating rate on the elemental distribution between phases in a low carbon steel. Eur J Mater. 2022;2:171–85. https://doi.org/10.1080/26889277.2022.2060761.
15. de Oro CR, Gierl-Mayer C, Danninger H. Thermoanalytical techniques for characterizing sintering processes in ferrous powder metallurgy. J Therm Anal Calorim. 2023;148:1309–20. https://doi.org/10.1007/s10973-022-11740-7.
16. Zurowski R, Gluszek M, Antosik A, Pietrzak E, Rokicki G, Szafran M. Copolymers dispersions designed to shaping of ceramic materials: Investigations of glass transition temperature, thermal stability and decomposition of water-thinnable binders. J Therm Anal Calorim. 2018;132:453–61. https://doi.org/10.1007/s10973-017-6955-3.
17. Wiecinska P. Thermal degradation of organic additives used in colloidal shaping of ceramics investigated by the coupled DTA/TG/MS analysis. J Therm Anal Calorim. 2016;123:1419–30.
18. O'Mahony C, Gkartzou E, Haq EU, Koutsoumpis S, Silien C, Charitidis CA, et al. Determination of thermal and thermomechanical properties of biodegradable PLA blends: for additive manufacturing process. J Therm Anal Calorim. 2020;142:715–22. https://doi.org/10.1007/s10973-020-09859-6.
19. Rijwani T, Ramkumar P. Thermal debinding for binder burnout in metal and ceramic processing. Heat Transf Eng. 2024. https://doi.org/10.1080/01457632.2024.2332111.
20. Zygmuntowicz J, Piątek M, Wachowski M, Piotrkiewicz P, Kaszuwara W. Thermoanalytical and dilatometric studies of the Al2O3–Cu–Mo hybrid composite. J Therm Anal Calorim. 2020;142:51–62. https://doi.org/10.1007/s10973-020-09526-w.
21. Lewis JA. Colloidal processing of ceramics. J Am Ceram Soc. 2004;83:2341–59.
22. Kovács TN, Hunyadi D, de Lucena ALA, Szilágyi IM. Thermal decomposition of ammonium molybdates. J Therm Anal Calorim. 2016;124:1013–21.
23. Maróti P, Varga P, Ferencz A, Ujfalusi Z, Nyitrai M, Lőrinczy D. Testing of innovative materials for medical additive manufacturing by DTA. J Therm Anal Calorim. 2019;136:2041–8.
24. Madarász J, Szilágyi IM, Hange F, Pokol G. Comparative evolved gas analyses (TG-FTIR, TG/DTA-MS) and solid state (FTIR, XRD) studies on thermal decomposition of ammonium paratungstate tetrahydrate (APT) in air. J Anal Appl Pyrolysis. 2004;72:197–201.
25. Kozień D, Graboś A, Nieroda P, Stępień J, Pasiut K, Gancarz P, et al. Spark plasma sintered TiB2-SiC UHTC derived from B4C and stoichiometric intermetallic phases from Ti-Si system. J Eur Ceram Soc. 2024;44:5401–14.
26. Irshad HM, Hakeem AS, Ahmed BA, Ali S, Ali S, Ali S, et al. Effect of Ni content and Al_2O_3 particle size on the thermal and mechanical properties of Al_2O_3/Ni composites prepared by spark plasma sintering. Int J Refract Met Hard Mater. 2018;76:25–32.
27. Vasylkiv O, Borodianska H, Sakka Y. Nanoreactor engineering and SPS densification of multimetal oxide ceramic nanopowders. J Eur Ceram Soc. 2008;28:919–27.
28. Borodianska H, Demirskyi D, Sakka Y, Badica P, Vasylkiv O. Grain boundary diffusion driven spark plasma sintering of nanocrystalline zirconia. Ceram Int. 2012;38:4385–9. https://doi.org/10.1016/j.ceramint.2011.12.064.

29. Bezdorozhev O, Borodianska H, Sakka Y, Vasylkiv O. Spark plasma sintered Ni-YSZ/YSZ bi-layers for solid oxide fuel cell. J Nanosci Nanotechnol. 2013;13:4150–7.
30. Martin E, Chung UC, Duttine M, Dourges MA, Clermont G, Labrugère C, et al. Defect chemistry to trigger zirconia densification at low temperatures by spark plasma sintering. Open Ceram. 2024. https://doi.org/10.1016/j.oceram.2023.100518.
31. Flaureau A, Weibel A, Chevallier G, Esvan J, Laurent C, Estournès C. Few-layered-graphene/zirconia composites: single-step powder synthesis, spark plasma sintering, microstructure and properties. J Eur Ceram Soc. 2022;42:2349–61.
32. Laurent C, Mesguich D, Séverac L, Tetihia R, Chevallier G, Estournès C. Iron-alumina composites: from discrete iron particles to interconnected iron network. Powder synthesis, spark plasma sintering, microstructure and mechanical properties. Open Ceram. 2023. https://doi.org/10.1016/j.oceram.2023.100485.
33. Tanska J, Wiecinski P, Kukielski M, Zygmuntowicz J, Wiecinska P. Coordination complexes as substitutes for metallic powders in ceramic-matrix-composites manufactured by aqueous colloidal processing: enhanced fracture toughness and quantitative microstructure analysis. J Eur Ceram Soc. 2023;44:341–52. https://doi.org/10.1016/j.jeurceramsoc.2023.08.059.
34. Zhou M, Liu W, Wu H, Song X, Chen Y, Cheng L, et al. Preparation of a defect-free alumina cutting tool via additive manufacturing based on stereolithography – optimization of the drying and debinding processes. Ceram Int. 2016;42:11598–602. https://doi.org/10.1016/j.ceramint.2016.04.050.
35. Zhao J. The use of ceramic matrix composites for metal cutting applications. Adv. Ceram. Matrix Compos. Woodhead Publishing Limited; 2014. https://doi.org/10.1533/9780857098825.3.537
36. Zhao Y, Mei H, Chang P, Yang Y, Cheng L, Zhang L. High-strength printed ceramic structures for higher temperature lubrication. Compos Part B Eng. 2021;221:109013. https://doi.org/10.1016/j.compositesb.2021.109013.
37. de Camargo IL, Morais MM, Fortulan CA, Branciforti MC. A review on the rheological behavior and formulations of ceramic suspensions for vat photopolymerization. Ceram Int. 2021;47:11906–21. https://doi.org/10.1016/j.ceramint.2021.01.031.
38. Porwal MK, Hausladen MM, Ellison CJ, Reineke TM. Biobased and degradable thiol-ene networks from levoglucosan for sustainable 3D printing. Green Chem. 2023;25:1488–502.
39. Simon U, Dimartino S. Direct 3D printing of monolithic ion exchange adsorbers. J Chromatogr A. 2019;1587:119–28. https://doi.org/10.1016/j.chroma.2018.12.017.
40. Guo W, Jiang Z, Zhang C, Zhao L, Jiang Z, Li X, et al. Fabrication process of smooth functionally graded materials through a real-time inline control of the component ratio. J Eur Ceram Soc. 2021;41:256–65. https://doi.org/10.1016/j.jeurceramsoc.2021.09.037.
41. Ngo TD, Kashani A, Imbalzano G, Nguyen KTQ, Hui D. Additive manufacturing (3D printing): a review of materials, methods, applications and challenges. Compos Part B Eng. 2018;143:172–96. https://doi.org/10.1016/j.compositesb.2018.02.012.
42. Jiang CP, Hsu HJ, Lee SY. Development of mask-less projection slurry stereolithography for the fabrication of zirconia dental coping. Int J Precis Eng Manuf. 2014;15:2413–9.
43. Lankford J. Indentation microfracture in the Palmqvist crack regime: implications for fracture toughness evaluation by the indentation method. J Mater Sci Lett. 1982;1(11):493–5.
44. Gu J, Li H, Wu Y, Huang S, Wu S, Chen D. Preliminary investigations on the catalytic hydrogenation of polycyclic aromatic hydrocarbons via WGSR. Mol Catal. 2021;515:111902. https://doi.org/10.1016/j.mcat.2021.111902.
45. Korth A, Marconi ML, Mendis DA, Krueger FR, Richter AK, Lin RP, et al. Probable detection of organic-dust-borne aromatic C3H3+ ions in the coma of comet Halley. Nature. 1989;337:53–5.
46. Zygmuntowicz J, Falkowski P, Miazga A, Konopka K. Fabrication and characterization of ZrO2/Ni composites. J Aust Ceram Soc. 2018;54:655–62.